RSC Advances

ROYAL SOCIETY OF CHEMISTRY

www.rsc.org/advances

GRAPHICAL ABSTRACT

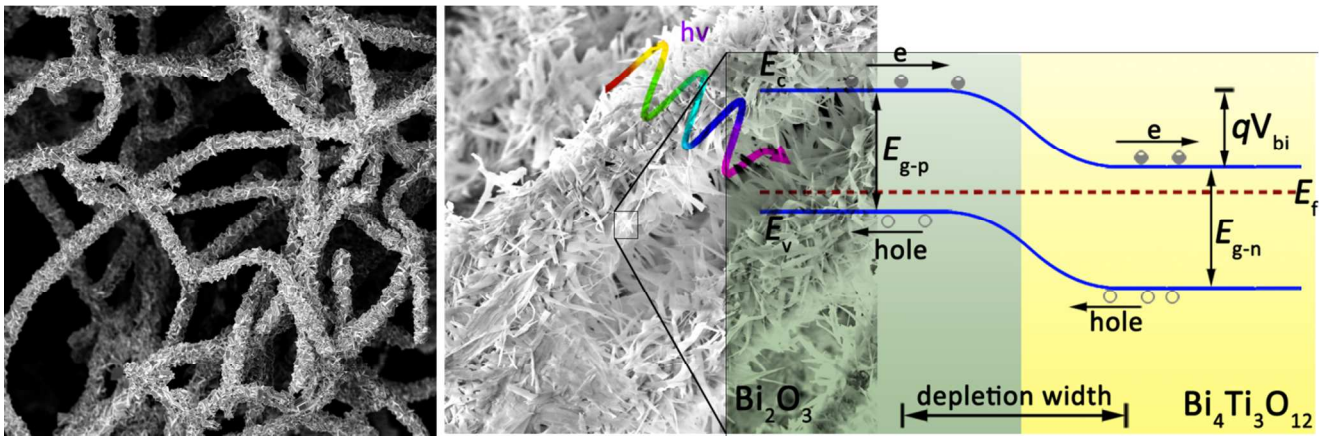

Synthesis of Hierarchical $Bi_2O_3/Bi_4Ti_3O_{12}$ p-n Junction Nanoribbons on Carbon Fibers from (001) Facets Dominated TiO_2 Nanosheets

Baicheng Weng*, [1], Fenghua Xu [1], Jianguang Xu

Materials Engineering Department, Yancheng Institute of Technology, 9 Xiwang Avenue, Yancheng, Jiangsu Province, 224051, China

***Corresponding Author**: baichengweng@gmail.com

[1]These authors contributed equally to this work.

Abstract

A novel hierarchical photocatalyst of $Bi_2O_3/Bi_4Ti_3O_{12}$ p-n junction nanoribbons (NRs) on carbon fibers has been successfully fabricated from the precursor of (001) facets dominated TiO_2 nanosheets (NSs), which provide well-shaped templates. The dominant (001) facets of TiO_2 precursor diminished slower than (101) facets during hydrothermal process. Single crystallized p-type Bi_2O_3 and n-type $Bi_4Ti_3O_{12}$ coexist forming p-n junctions within one NR. This hierarchical nanostructure exhibits markedly improved photocatalytic activity for degradation of methyl orange. The improvement can be attributed to enhanced absorption in the visible light region due to the ultrathin NRs, more efficient charge separations/transportations owing to the formation of p-n junction, and high exposure of reactive (001) facets resulting from the formation of hierarchical structure. Moreover, this hierarchical photocatalyst shows high stability and excellent recycled property.

Keywords: Hierarchical nanostructure, Photocatalysis, P-n junction, Facets, Nanoribbons

Introduction

Semiconductor photocatalysis possesses potentials of providing a promising pathway for solving energy supply and environmental pollution problems.[1] Many photocatalysts have been developed since the photocatalytic activity of TiO_2 was found.[2-7] The bismuth-based semiconductors having d^{10} metal cations, such as Bi_2O_3, BiOCl, $BiVO_4$ and $Bi_4Ti_3O_{12}$, usually consist of O 2p molecular orbitals serving as the top of valence band, and the hybridized s, p orbitals as well as the d-band of typical metals serving as the bottom of conduction band.[8] The band position of O 2p molecular orbitals usually locates at around +3 V (vs. NHE) which is below the potential for water oxidation (1.23 V vs. NHE), rendering their high potentials for water splitting and photocatalytic oxidation.[9] Incorporation of metals into Bi-O semiconductors changes the hybridized s, p orbitals as well as valance band and hence brings unique properties according to the amount of metal incorporated. Especially, bismuth titanates (Bi-Ti-O) have drawn many attentions due to their various phases including $Bi_4Ti_3O_{12}$, $Bi_2Ti_2O_7$, $Bi_2Ti_4O_{11}$, $Bi_{12}TiO_{20}$ and $Bi_{20}TiO_{32}$, and each of them has unique electronic and optical properties.[10-13] For instance, $Bi_2Ti_2O_7$ and $Bi_4Ti_3O_{12}$ exhibit relatively higher photocatalytic activities, but higher band gaps. In contrast, $Bi_{20}TiO_{32}$ has a broader light absorption extended to visible light region; however, it usually appears in low catalytic metastable phase.[13]

Bismuth-based semiconductors with large grain sizes, however, have some disadvantages, such as small specific surface areas and relatively high recombination rates of charge carriers, which adversely affects the photocatalytic activities.[14] The reduction of semiconductor size to nanoscale could offer an effective way to solve the above-mentioned problems. Recently, quasi-two-dimensional nanomaterials have attracted intensive interest, because their unique structures can provide high specific surface area, large fraction of uncoordinated surface atoms and low atom affinity of the exposed atoms on the surface compared to their bulk counterparts,[15] and the separation of their crystal facets can highly expose reactive facets, favoring the separation of photo-generated carriers.[16] However, the nanostructures also suffer from insufficient band bending due to the size reduction, which means insufficient driving force for charge transportation and inefficient charge separations, compromising the photocatalytic improvements.[17, 18]. Unique structures, such as heterojunctions, p-n junction and oriented polarization, could provide effective ways to overcome this drawback.[17-19] It is worth noticing that the formation of p-n junction within single nanosheet (NS) or nanoribbon (NR) has rarely reported yet. Moreover, nanostructure powders or granular supported nanostructures are difficult to be recycled from photocatalytic solutions and cannot

fully expose reactive facets. One effective way to improve the regenerability is synthesizing the nanostructures on carbon fibers (CFs) forming a hierarchical structure. One-dimensional CFs have been widely used as ideal electron collectors and transporters due to their 1-d conductivity, good chemical resistance and flexibility.[20] More importantly, the hierarchical CFs supported nanostructures can supply large surface area to fully expose the reactive facets compared to the powders, which is critical for nanostructure-based photovoltaic and photocatalytic technology.

In this study, we report a novel hierarchical structure of $Bi_2O_3/Bi_4Ti_3O_{12}$ p-n junction NRs attached onto the CFs synthesized by using CFs supported TiO_2 NSs with dominant (001) facets as the precursor. During the hydrothermal process, Bi ions stabilize (001) facets, which supply a well-shaped template for synthesis of the ultrathin p-n junction NRs. Although it is under intensive studies for preparation of facets dominated TiO_2 nanostructures, synthesis and tailoring the morphology of Ti-O based quasi-two-dimensional nanomaterials from facet dominated TiO_2 NSs have rarely been reported.

Experimental Section

Synthesis of the hierarchical structure: CFs supported TiO_2 NSs were firstly prepared.[20] Typically, 1.0 mL $Ti(OBu)_4$ was slowly dropped into 18 mL 5.0 M HCl, followed by vigorously stirring for 30 min, 0.5 mL HF was then added to the solution. The solution and the CFs were transferred into a hydrothermal autoclave at 180 ^oC for 5 h. After the autoclave was cooled to room temperature by quenching with water, the samples were ultrasonically cleaned for 3 min in a 2:1 (v/v) mixture of isopropyl alcohol and DI water, and dried under vacuum. The hierarchical structure of p-n junction NRs on the CFs was synthesized using the as-prepared TiO_2 NSs as the precursor. $Bi(NO_3)_3•5H_2O$ was added into 15.0 mL 1.0 M NaOH solution under vigorously stirring for 1 h until The color became yellow, followed by immersing CFs supported TiO_2 NSs precursors in the solution. The hydrothermal synthesis was conducted at 180 ^oC for 48 h. After the autoclave was cooled to room temperature naturally, the samples were ultrasonically cleaned for 3 min in a 2:1 (v/v) mixture of isopropyl alcohol and DI water, and dried under vacuum again. For comparison, $Bi_2O_3/Bi_4Ti_3O_{12}$ p-n junction NR powder was prepared using the same procedure in the absence of CFs. Bi_2O_3 NSs were also synthesized using the same method without TiO_2 precursor, and $Bi_4Ti_3O_{12}$ NSs were prepared using TiO_2 NS powder as precursor at a molar ratio of 4:3 for $Bi(NO_3)_3$:TiO_2.

Characterization: The morphology of the samples was evaluated using a scanning electron microscope (SEM, Sigma VP, Carl Zeiss, Germany) coupled with an energy-dispersive X-ray spectrometer (EDS). Powder X-ray diffraction patterns (XRD) were recorded on Bruker D8 Advance ECO diffractometer equipped with graphite monochromatized high-intensity Cu Kα radiation (λ=1.54178Å). The transmission electron microscopy (TEM), high-resolution transmission electron microscopy (HRTEM) and the corresponding selected-area electron diffraction (SAED) images were taken on a JEOL-2010 TEM operated at an acceleration voltage of 200kV. X-ray photoelectron spectra (XPS) were collected on a physical electronics PHI5400 using Mg Ka radiation as the X-ray source. The elemental analyses were conducted using an inductively coupled plasma optical emission spectroscopy (ICP-OES, ICAP-6300, Thermo Fisher, USA). UV-visible diffuse reflectance spectra were conducted on Perkin-Elmer Lambda 950 UV-vis-NIR spectrophotometer with an integrating sphere. The specific surface area was calculated from the 0.1- 1.0 p/p_0 region of the adsorption isotherm using the Brunauer-Emmett-Teller (BET) method. The Mott-Schottky was conducted in 0.5 M Na_2SO_4 using Gamry 600 potentiostats at a frequency of 1, 000 Hz, with Pt as counter electrode and Ag/AgCl as reference electrode. The electrochemical impedance spectroscopy was conducted at frequencies of 300 kHz to 1 Hz in 0.5 M Na_2SO_4 with 20 ppm MO addition with Pt as counter electrode and Ag/AgCl as reference electrode.

Photocatalytic evaluation: The photocatalytic activity was evaluated using MO aqueous solution at ambient temperature. A sunlight simulator lamp with AM 1.5 filter (Au Light Co, Ltd, China) was used as the light source. Prior to irradiation, all the samples ($1gL^{-1}$) were immersed in the MO solution with initial concentration of 20 mg L^{-1} and kept in the dark for 2 h to make sure that absorption/desorption equilibrium was established. The absorbance changes of MO were monitored by measuring the maximal absorption at 465 nm using a UV–vis spectrophotometer. For the regeneration test of the photocatalyst, 10 consecutive cycles were tested, and the samples were washed thoroughly with DI water and dried after each cycle.

Results and Discussion

TiO_2 NSs were firstly synthesized on the CFs,[20] and served as the precursor for growth of $Bi_2O_3/Bi_4Ti_3O_{12}$ NRs in a high pH bismuth aqueous solution. As indicated in Figure 1a-c, after the first step hydrothermal reaction, the CF surface was uniformly covered by tetragonal TiO_2 NSs with a thickness of 300 nm and a length of 2.8 - 3.3 μm forming a hierarchical structure. The as-prepared TiO_2 NSs are composed of (001) and (101) facets (Figure 1c). The laminar morphology of the (001) facets reflects the faster growth rate along *x*-axis directions than *z*-axis directions ((101) facets).[20] XRD measurement (Figure S1a) shows that the as-prepared NSs are well-crystallized anatase TiO_2. Following the second step hydrothermal reaction of TiO_2 NSs in high pH bismuth aqueous solution, the $Bi_2O_3/Bi_4Ti_3O_{12}$ NRs uniformly attached onto the surface of CFs were obtained. The $Bi_2O_3/Bi_4Ti_3O_{12}$ NRs are different from TiO_2 NSs and feature a leaf-like morphology with a thickness around 8 nm, a width of 250 - 560 nm and a length of 1.3 - 2 μm (Figure 1d-g).

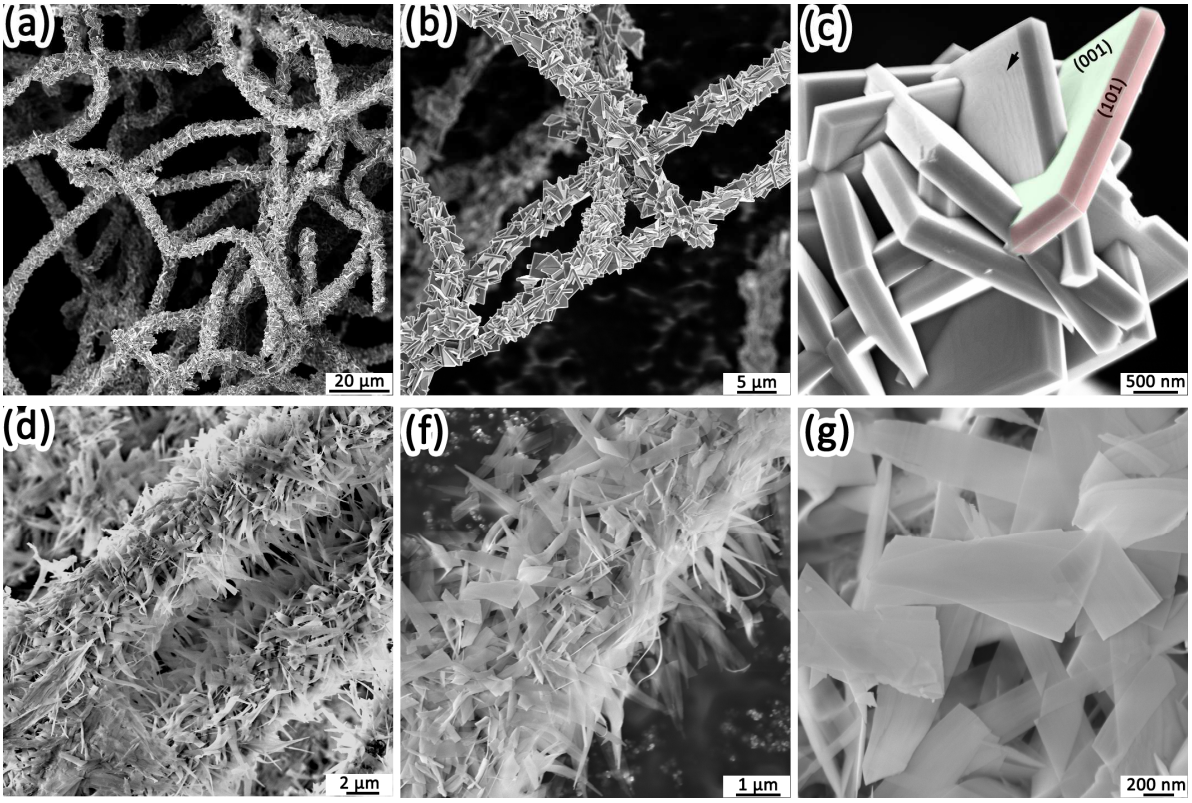

Figure 1. SEM images of the hierarchical $Bi_2O_3/Bi_4Ti_3O_{12}$ p-n junction NRs on CFs (d-g) and their precursors of TiO_2 NSs (a-c). The laminar structure of the (001) facets of TiO_2 NSs is labeled with arrow.

The XRD measurements (Figure S1a) confirm that the as-prepared CFs supported NRs are composed of cubic δ-phase Bi_2O_3 and orthorhombic $Bi_4Ti_3O_{12}$. Bi_2O_3 is an amphoteric semiconductor with four kinds of crystal structures and each of them has unique band structures. Among them, the fcc δ-phase and the monoclinic α-phase are p-type semiconductors,[21] while $Bi_4Ti_3O_{12}$ is an n-type semiconductor. Therefore, p-n junction is formed within the $Bi_2O_3/Bi_4Ti_3O_{12}$ NRs. The EDS analysis (Figure S1b) shows the elements in the NRs are only Bi, Ti and O, and the molar ratio of Bi/Ti in the NRs is 2.72, corresponding to 2:1 for $Bi_2O_3/Bi_4Ti_3O_{12}$. Moreover, quantitative analyses of Bi and Ti elements by ICP-OES further confirm the EDS result. The sample was subjected to XPS studies to further identify the surface composition and chemical state. The survey XPS spectrum (Figure 2a) reveals the presence of Bi, Ti and O elements. Figure 2b-d shows the high-resolution XPS spectra of Bi 4f, O 1s, Bi 4d and Ti 2p core level peaks, respectively. The peaks at 158.8 and 164.1 eV (Figure 2b) are corresponding to Bi $4f_{7/2}$ and $4f_{5/2}$, respectively with a typical Bi 4f spin-orbit splitting of 5.3 eV, which is characteristic of Bi^{3+} in Bi_2O_3 and $Bi_4Ti_3O_{12}$. The peak of O 1*s* (Figure 2c) are contributed by the surface adsorbed oxygen and lattice oxygen of Bi–O and Ti–O bonds at 530.9 eV, 529.7 eV and 530.0 eV, respectively. The peaks at 457.0 and 462.7 eV (Figure 2d) are assigned to Ti $2p_{3/2}$ and Ti $2p_{1/2}$, respectively with a typical Ti 2*p* spin-orbit splitting of 5.7 eV, which is characteristic of Ti^{4+} in $Bi_4Ti_3O_{12}$. In addition, the peaks of Ti $2p_{1/2}$ and Bi $4d_{3/2}$ are partially overlapped to a broad bump around 465.0 eV. The XPS observations further confirm the coexistence of Bi_2O_3 and $Bi_4Ti_3O_{12}$ in the NRs, which agrees well with the XRD result. The HRTEM images (Figure 3) reveal that the NR is composed of two kinds of lattice fringes. In selected area A, the lattice spacings of the two set of lattices marked in the image are 0.282 and 0.282 nm oriented perpendicular to each other, corresponding to (200) and (020) atomic planes of cubic Bi_2O_3. In selected area B, two perpendicular lattice spacings are 0.270 and 0.272 nm, corresponding to (020) and (200) atomic planes of orthorhombic $Bi_4Ti_3O_{12}$. The corresponding selected area electron diffraction (SAED) patterns reveal $Bi_2O_3/Bi_4Ti_3O_{12}$ p-n junction NRs are in single crystalline nature, and dominated with fully exposed (001) facets.

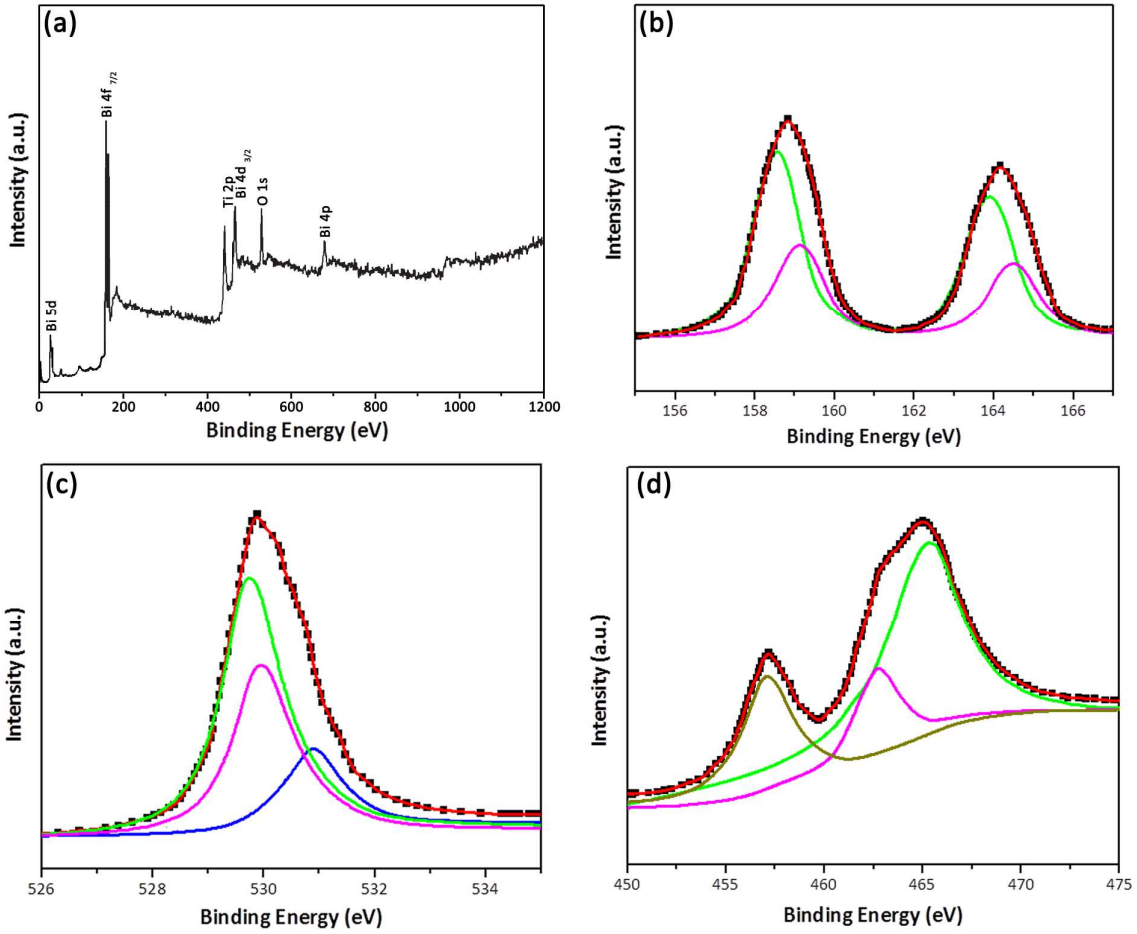

Figure 2. (a) Survey XPS spectrum of the $Bi_2O_3/Bi_4Ti_3O_{12}$ NRs. High-resolution XPS spectra of (b) Bi4f, (c) O 1s, and (d) Bi 4d, Ti 2p.

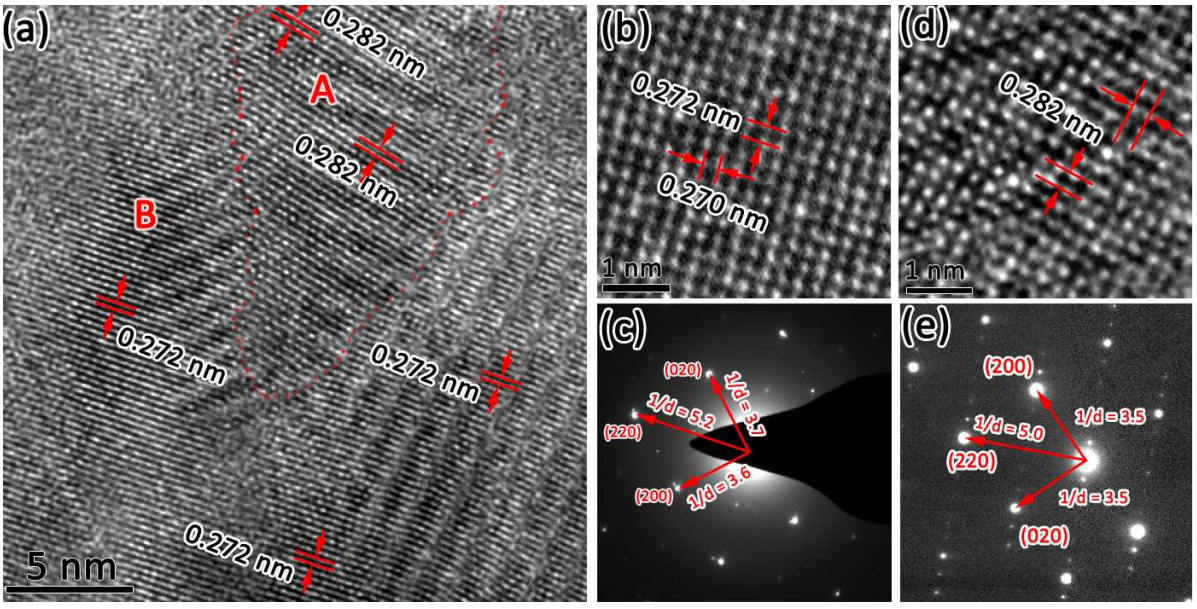

Figure 3. HRTEM (a, b, d) and the corresponding SAED patterns (c, e) of $Bi_2O_3/Bi_4Ti_3O_{12}$ p-n junction NRs with two kinds of crystal lattices (Bi_2O_3 and $Bi_4Ti_3O_{12}$). (b) and (d) are the HRTEM images of area B and A in high magnification, and (c) and (e) are the corresponding SAED patterns, respectively. The lattice margins are labeled with dash lines.

It is worthy to note that the as-prepared intermediate nanostructures attached onto the surface of CFs have the similar orientation with their precursor of TiO_2 NSs after the first 3 and 10 h hydrothermal reactions (Figure S2, labeled with red lines). Moreover, it is observed that the thickness of these intermediate nanostructures remarkably decreases, indicating the faster dissolution of (101) facets than (001) facets, although their size also slightly shrinks, showing the slight dissolution of (001) facets. It is well known that the (001) facets of the TiO_2 NSs are thermodynamically more unstable than (101) facets during the hydrothermal reaction, due to their higher average surface energies (0.90 ~ 0.93 J m^{-2}) than (101) facet (0.39 ~ 0.44 J m^{-2}) and high density of surface under coordinated Ti atoms and very strained configuration of the surface atoms, specifically, the large Ti–O–Ti bond angles.[21, 22] Therefore, in the hydrothermal process, TiO_2 will firstly dissolve, and then experience a downhill reaction to form nanoparticles or nanowires and (001) facets are expected to diminish faster than (101) facets, driven by the Gibbs free energy difference to minimize the surface energy.[22-27] To prepare (001) facets dominated TiO_2 NSs, ionic additives (*e.g.* F^-) or surfactants are usually employed, due to the absorption and strong covalent/non-covalent interaction of these additives with the (001) facets of TiO_2 nanostructures.[21-23] The bindings of the atoms from the additives with Ti/O are stronger than these of Ti-O and O-O, which effectively stabilizes the (001) facet.[24] In this study, neither surfactants nor F^- ions were used, but it was still observed that the (001) facets diminished slower than (101) facets. Therefore, Bi ions is speculated to play an important role in stabilizing the (001) facets. Bi-Ti bonds preferably form on the reactive (001) facets, and then stabilize the (001) facets and prevent the dissolution of the (001) facets. The unreactive (101) facets keep dissolving rather than recrystallizing during the hydrothermal reaction process, especially for the reaction route comprising fast dissolution and slow crystallization processes in high alkaline solutions.[22-24] Therefore, during the hydrothermal process, the stabilized (001) facets of the TiO_2 NSs provide well-shaped templates for synthesis of ultrathin p-n junction NRs with the continuous insertion of Bi_2O_3. The schematic illustration for the synthetic process of hierarchical CFs supported $Bi_2O_3/Bi_4Ti_3O_{12}$ NRs is shown in Figure 4. TiO_2 NSs were firstly grown on the surface of CFs by the first step hydrothermal reaction, and served as

the precursor. During the second hydrothermal process, Bi ions stabilized (001) facets of the TiO_2 NSs, while the (101) facets diminished quickly. Meanwhile, Bi_2O_3 continuously inserted into the nanostructures resulting in the conversion of TiO_2 NSs to ultrathin $Bi_2O_3/Bi_4Ti_3O_{12}$ NRs.

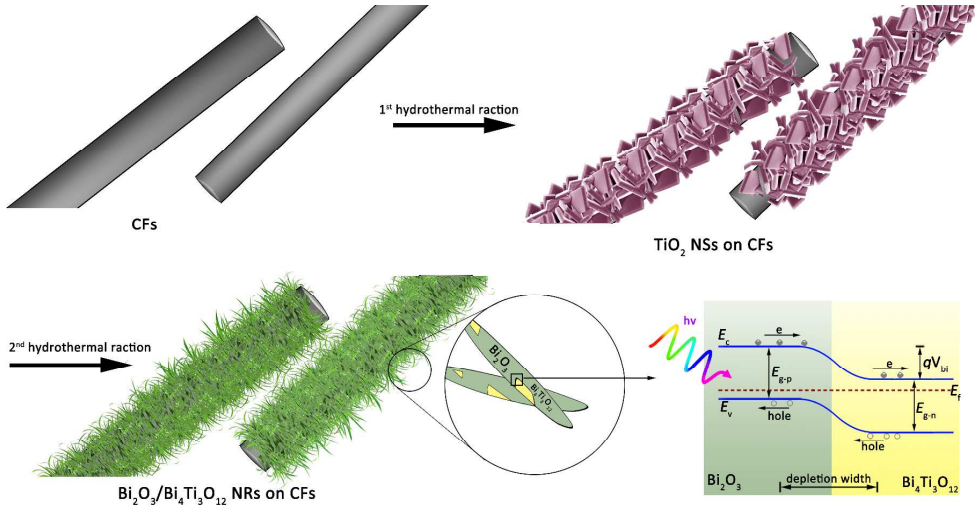

Figure 4. Schematics of the preparation of hierarchical $Bi_2O_3/Bi_4Ti_3O_{12}$ p-n junction NRs on CFs and the formation of p-n junction within one NR and the charge transfer and separation process of p-n junction NR under irradiations.

The photocatalytic activities of the as-prepared hierarchical p-n junction NRs on CFs were evaluated by degradation of methyl orange (MO) under simulated sunlight, and Bi_2O_3 and $Bi_4Ti_3O_{12}$ NSs prepared under the same conditions for comparison (Figure 5). The dependence of the concentration of MO on the irradiation times follows the first-order kinetics well (Figure 5b), $-\ln(C/C_0) = kt$, where t is the irradiation time and k is the rate constant.[28] It is found that the Bi_2O_3 and $Bi_4Ti_3O_{12}$ NSs have similar degradation ability and their corresponding rate constants are 0.008 and 0.010 min^{-1}, respectively, whereas the $Bi_2O_3/Bi_4Ti_3O_{12}$ p-n junction NRs have much higher photocatalytic activity (0.039 min^{-1}), 4-fold higher than that of Bi_2O_3 and $Bi_4Ti_3O_{12}$ NSs, which may be attributed to the formation of p-n junction within the NRs. In contrast, the hierarchical CFs supported p-n junction NRs have an even higher photocatalytic degradation rate constant of 0.119 min^{-1}, more than 3-fold higher than the p-n junction NR powders. These results show that the remarkable enhanced photocatalytic activity for the $Bi_2O_3/Bi_4Ti_3O_{12}$ NRs on CFs is attributed to the formation of both p-n junction and the hierarchical structure.

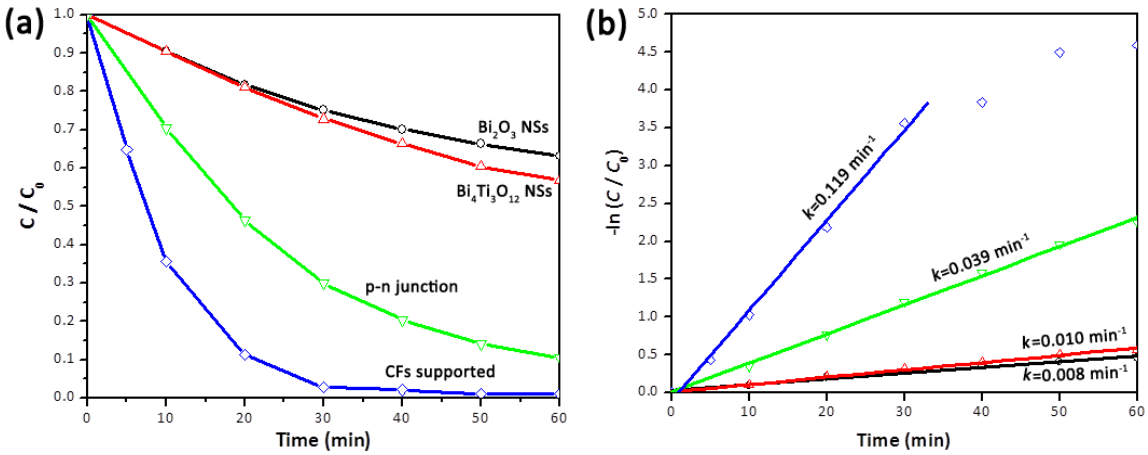

Figure 5. MO degradation profiles (a) of Bi_2O_3 NSs, $Bi_4Ti_3O_{12}$ NSs, $Bi_2O_3/Bi_4Ti_3O_{12}$ p-n junction NRs and hierarchical CFs supported p-n junction NRs, respectively, and the corresponding kinetic linear curves (b).

The energy band structure is considered to be one of key factors that determine a semiconductor's photocatalytic behavior, because it can affect the light absorptions and the effective density of light-induced carriers. Figure 6a displays the UV-visible absorption spectra in the wavelength range of 300 - 800 nm for the as-prepared products, and Bi_2O_3 and $Bi_4Ti_3O_{12}$ NSs prepared under the same conditions and their corresponding bulk powders are for comparison. Bi_2O_3 has broader absorptions than $Bi_4Ti_3O_{12}$, due to its narrower energy gaps. Specifically, Bi_2O_3 exhibits light absorption edges of 456 and 464 nm for bulk powders and NSs, respectively. While $Bi_4Ti_3O_{12}$ shows absorption edges at 413 and 424 nm for bulk powders and NSs, respectively. Therefore, Bi_2O_3 and $Bi_4Ti_3O_{12}$ NSs show noticeable light absorption redshifts of 8 nm and 11 nm, respectively, compared to their bulk powder counterparts. Contrastively, p-n junction NRs exhibit light absorption between the absorption regions of Bi_2O_3 and $Bi_4Ti_3O_{12}$ NSs at wavelength below 430 nm, which may be ascribed to the existence of $Bi_4Ti_3O_{12}$ in the NRs, but their light absorption at high wavelength is remarkably enhanced, especially, for the hierarchal CFs supported sample. As shown in Figure 6b, the energy gaps are calculated to be 2.69 eV and 2.97 eV for Bi_2O_3 and $Bi_4Ti_3O_{12}$ NSs, respectively, while their corresponding bulk powders are 2.71 eV and 3.03 eV, respectively. The smaller energy gaps mean enhanced light absorptions and higher density of light-induced carriers. On the other hand, the smaller energy gaps also suggest an increase in conduction band (CB) and valence band (VB) edge positions according to the following equations: $E_{CB} = X - 4.5$ eV $- 1/2\ E_g$, $E_{VB} = E_{CB} + E_g$, where E_{CB} and E_{VB} are the band edge positions, X is the electronegativity of the semiconductor, and E_g is the energy gap obtained from Tauc plot.

The calculation of E_{CB} and E_{VB} reveals up-shifts of 0.01 eV and 0.03 eV for $Bi_4Ti_3O_{12}$ NSs, and 0.03 eV and 0.09 eV for Bi_2O_3 NSs, respectively, which reflects the enhancements in efficacy of holes and the decreased barriers of electron (reduction in electrons affinity, $E_A = E_0 - E_{CB}$). Therefore, higher oxidation activities and facilitated transportation of photoexcited electrons to reactants could be expected.[29]

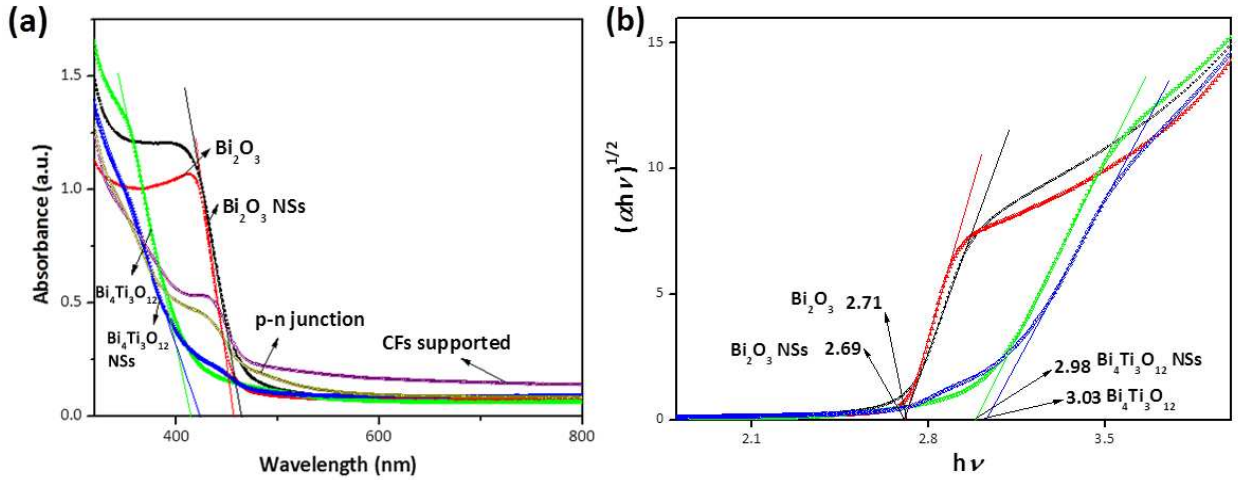

Figure 6. UV-vis absorption spectra (a) of Bi_2O_3 NSs, $Bi_4Ti_3O_{12}$ NSs, $Bi_2O_3/Bi_4Ti_3O_{12}$ p-n junction NRs and hierarchical CFs supported p-n junction NRs, respectively, and the corresponding energy gap plots estimated by a related curve of $(\alpha h\nu)^{1/2}$ versus photon energy ($h\nu$) (b).

Single phase nanostructured semiconductors are usually lack of sufficient band bending due to the size decrease, indicating the insufficient potential barriers at the interface between the semiconductor and electrolyte.[17-19] Thereby the electrons transport to the surface mainly through diffusion rather than drift, and the lack of sufficient band bending would slow down the transportation and collection of majority carriers.[17-19] However, for p-n junction nanostructures, a built-in potential created through p-n junction will provide an electrical driving force for separation and transportation of charges. Mott-schottky studies for Bi_2O_3 and $Bi_4Ti_3O_{12}$ NSs were conducted to further verify the type and flat band potential. Mott−Schottky plots are generated from the capacitance values. As shown in Figure 7, Bi_2O_3 NSs show a negative slope, while the $Bi_4Ti_3O_{12}$ NSs show a positive slope, indicating that Bi_2O_3 is a p-type semiconductor with electrons as majority carriers and $Bi_4Ti_3O_{12}$ is an n-type semiconductor with holes as majority carriers. The flat band potential can be calculated using the Mott-schottky equation $1/C^2 = 2(V_{appl}-V_{fb}-k_BT/e)/(\varepsilon\varepsilon_0A^2eN_d)$, where C is the specific capacitance (F/cm^2), e the electron charge, ε the dielectric constant, ε_0 the

permittivity of vacuum, N_d the donor density, V_{appl} the electrode applied potential, V_{fb} the flat band potential, A the surface area and k_BT/e has usual significance. By extrapolating the X-intercepts of the linear region in Mott-Schottky plots ($1/C^2$ vs. V), V_{fb} of Bi_2O_3 and $Bi_4Ti_3O_{12}$ NSs are found to be -0.1 V and -0.7 V (vs. SCE), respectively. Therefore, upon the equilibrium, the alignment of Fermi levels in the p-n junction can create a built-in potential (V_{bi}) of 0.6 V. This built-in potential is capable of generating a depletion region of 8.9 μm at equilibrium according to the equation $W = (2\varepsilon_r\varepsilon_0(N_A+N_D)V_{bi}/qN_AN_D)^{1/2}$, where ε_r and ε_0 are dielectric constant of the semiconductor and vacuum permittivity, respectively. N_A and N_D are the number of ionized donors and acceptors, respectively, which can be interpreted from the gradual slop of Mott-Schottky plots in linear sections. It is worthy to note that this depletion region is much larger than the size of the NR (8 nm in thickness and 2 μm in length), which is beneficial for charge separation in the depletion regions driven by the built-in potential. Therefore, the diffusion length of photogenerated charge carriersscan be enhanced and their recombination can be inhibited, resulting in higher photocatalytic activities. The Electrochemical Impedance Spectroscopy (EIS, Figure S3) further confirms that the p-n junction NRs can effectively promote the separation and transportation of the charges. Due to the faster charge transfer inside the semiconductor than at the semiconductor/electrolyte interface, high frequency response is assigned to the electronic process in the semiconductor and the resistance of the solution, whereas medium and low frequency response is assigned to the interfacial charge-transfer resistance between the semiconductor and electrolyte, which shows one dominant semicircle, whose diameter is related to charge-transfer resistance at the semiconductor/electrolyte interface. Smaller diameter of the semicircle means smaller impedance in charge separation and transportation. The solution for EIS test is 0.5 M Na_2SO_4 with addition of 10 ppm MO. Under small amplitude (10 mV) of the applied EIS potential, only the degradation reaction of MO occurs on the sample surface. Therefore, the measured interfacial charge-transfer resistance (R_{ct}), calculated from the middle frequency of the Nyquist diagrams is resistance for MO degradation. Bi_2O_3 and $Bi_4Ti_3O_{12}$ NSs have relatively high R_{ct} of 1124 and 1436 Ω respectively, while the R_{ct} of p-n junction NRs remarkably decreases to 418 Ω, indicating that p-n junction NRs possess more efficient charges separation. The EIS of p-n junction NRs also displays concentration polarization at low frequency, indicating faster surface reaction than reactants transfer.

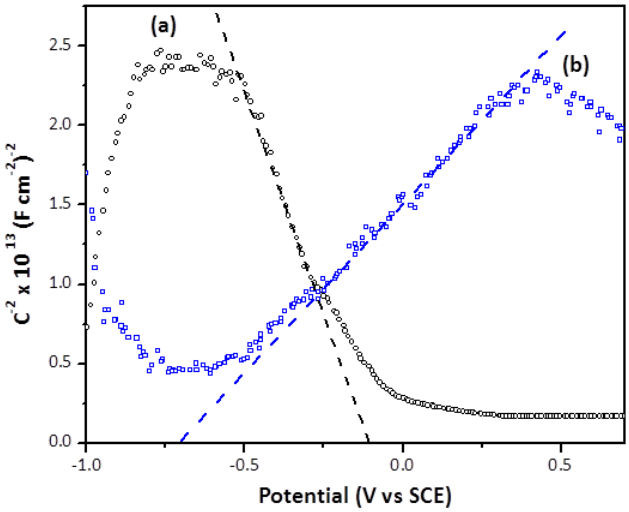

Figure 7. Mott–Schottky plots of Bi_2O_3 NSs (a) and $Bi_4Ti_3O_{12}$ NSs (b), respectively.

The full exposure of effective surface will play an important role in determining the photocatalytic performance. The BET analyses (Figure S4) reveal a specific surface area of 41.26 $m^2\ g^{-1}$ for the hierarchical CFs supported p-n junction NRs, while the NR powders only have a surface area of 16.02 $m^2\ g^{-1}$. The result shows that the supporting materials of CFs with a large surface area (76.81 $m^2\ g^{-1}$) can effectively support the NRs, and are able to expose more reactive facets of the NRs in a radial distribution when supporting NRs than neat NRs.[20] As a result, the hierarchical CFs supported p-n junction NRs exhibit more than 3-fold improvement in photocatalytic activity, compared with p-n junction NR powders, while p-n junction NRs have 4-fold greater photocatalytic activity than that of Bi_2O_3 and $Bi_4Ti_3O_{12}$ NSs (Figure 5), indicating that the great improvement in photocatalytic activity benefits from both the formation of p-n junction and high exposure reactive (001) facets. Moreover, the regeneration of the photocatalyst is one of the major factors for a catalyst to be used in the practical applications. The supporting materials, CFs could enhance the regeneration properties of their supported nanostructures, due to the excellent mechanical and chemical resistance properties of the CFs.[20] The cyclic performance of the hierarchical $Bi_2O_3/Bi_{20}TiO_{32}$ p-n junction NRs on CFs is shown in Figure 8. The photocatalytic degradation of MO was monitored for 10 consecutive cycles and each cycle lasted 60 min. After each cycle, aqueous solution was removed, and the samples were washed with deionized (DI) water for 4 times, and then fresh MO solution was refilled and kept for 2 h before carrying out the next cycle. It is found that the photocatalytic activities keep unchanged up to 10

cycles, which suggests the noticeable stability and good recycled ability of this hierarchical photocatalyst.

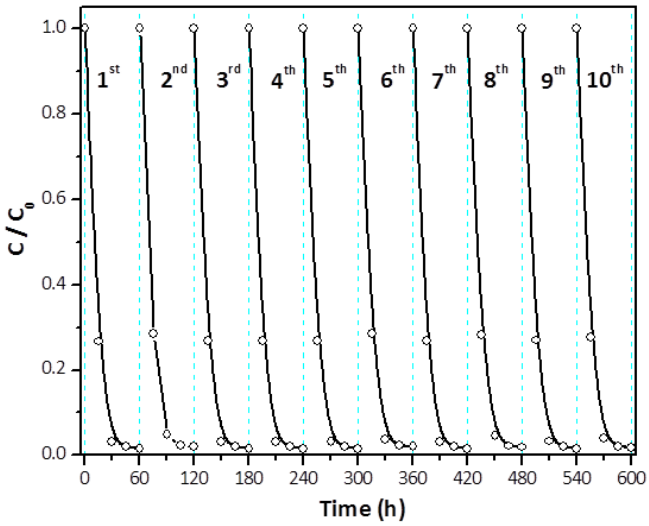

Figure 8. Cycling curves of photocatalytic degradation of MO with the hierarchical CFs supported $Bi_2O_3/Bi_4Ti_3O_{12}$ p-n junction NRs for 10 cycles.

Conclusions

In summary, a novel hierarchical structure of $Bi_2O_3/Bi_4Ti_3O_{12}$ p-n junction NRs on the surface of CFs has been fabricated for the first time by hydrothermal reaction of Bi ions with CFs supported TiO_2 NSs with dominant (001) facets. The differentiated dissolving behaviors among the facets of TiO_2 NSs provide a well-shaped seed for synthesis of ultrathin p-n junction NRs. The hierarchical CFs supported p-n junction NRs show remarkably improved photocatalytic activities and good recyclable ability, due to facilitated charge separations/transportations, enhanced light absorption and improved surface areas. Herein, we offer broad insight into the effect of facet of semiconductors on hydrothermal reactions. Also, this facile synthetic route in this study provides a novel pathway for synthesis of hierarchical p-n junction nanomaterials and the development of stable, efficient and recycled photocatalysts for applications in water splitting, photocatalysis, solar cells and gas sensoring.

Acknowledgments

This work was financially supported by the National Natural Science Foundation of China (Grant No. 51202281) and shanghai Natural Science Foundation (11ZR1444300).

References

[1] E. Borgarello, J. kiwi, E. Pelizzetti, A. Visca, M. Grätzel, *Nature* 1981, **289**, 158-160.

[2] A. Fujishima, K. Honda, *Nature* 1972, **238**, 37-38.

[3] S. Ida, A. Takashiba, S. Koga, H. Hagiwara, T. Ishihara, *J. Am. Chem. Soc.* 2014, **136**, 1872-1878.

[4] W. Wang, J. Wang, Z. Wang, X. Wei, L. Liu, Qi. Ren, W. Gao, Y. Liang, H. Shi, *Dalton Trans*. 2014, **43**, 6735-6743

[5] J. Yu, J. Low, W. Xiao, P. Zhou, M. Jaroniec, *J. Am. Chem. Soc.* 2014, **136**, 8839-8842.

[6] A. Hao, S. Cao, P. Zhou, J. Yu, *Chinese J. Catal.* 2014, **35**, 989-1007.

[7] H. Lin, H. Ye, B. Xu, J. Cao, S. Chen, *Catal. Commun*. 2013, **37**, 55-59.

[8] G. Blasse, G. J. Dirksen, P. H. M. de Korte, *Mater. Res. Bull.* 1981, **16**, 991-998.

[9] D. N. Ke, T. Y. Peng, L. Ma, P. Cai, P. Jiang, *Appl. Catal. A* 2008, **350**, 111-117.

[10] J. Jin, J. Yu, G. Liu, P. K. Wong, *J. Mater. Chem. A* 2013, **1**, 10927-10934.

[11] Z. Yang, H. Q. Fan, X. Wang, C. B. Long, *J. Phys. Chem. Solids* 2013, **74**, 1739-1744.

[12] X. Q. Zhu, J. L. Zhang, F. Chen, *Appl. Catal. B* 2011, **102**, 316-322.

[13] Y. Y. Li, L. Y. Dang, L. F. Han, P. P. Li, J. S. Wang, Z. J. Li, *J. Mol. Catal. A* 2013, **379**,146-151.

[14] J. Di, J. Xia, S. Yin, H. Xu, L. Xu, Y. Xu, M. He, H. Li, *J. Mater. Chem. A* 2014, **2**, 5340-5351.

[15] M. Guan, C. Xiao, J. Zhang, S. Fan, R. An, Q. Cheng, J. Xie, M. Zhou, B. Ye, Y. Xie, *J. Am. Chem. Soc.* 2013, **135**, 10411-10417.

[16] R. Li, F. Zhang, D. Wang, J. Yang, M. Li, J. Zhu, X. Zhou, H. Han, C. Li, *Nat. Comm.* 2013, **4**, 1432.

[17] J. J. Kelly, D. Vanmaekelbergh, *Electrochim. Acta* 1998, **43**, 2773-2780.

[18] A. Zaban, A. Meier, B. A. Gregg, *J. Phys. Chem. B* 1997, **101**, 7985-7990.

[19] H. Wang, T. You, W. Shi, J. Li, L. Guo, *J. Phys. Chem. C* 2012, **116**, 6490-6494.

[20] W. Guo, F. Zhang, C. Lin, Z. Wang, *Adv. Mater.* 2012, **24**, 4761-4764.

[21] K. L. Hardee, A. J. Bard, *J. Electrochem. Soc.* 1977, **124**, 215-224.

[22] H. G. Yang, C. H. Sun, S. Z. Qiao, J. Zou, G. Liu, S. C. Smith, H. M. Cheng, G. Q. Lu, *Nature* 2008, **453**, 638-642.

[23] C. Z. Wen, H. B. Jiang, S. Z. Qiao, H. G. Yang, G. Q. (M.) Lu, *J. Mater. Chem.* 2011, **21**, 7052-7061.

[24] A. Selloni, *Nature Mater.* 2008, **7**, 613-615.

[25] J. Yang, Z. Jin, X. Wang, W. Li, J. Zhang, S. Zhang, X. Guo, Z. Zhang, *Dalton Trans.* 2003, 3898-3901.

[26] D. V. Bavykin, V. N. Parmon, A. A. Lapkin, F. C. Walsh, *J. Mater. Chem.* 2004, **14**, 3370-3377.

[27] D. V. Bavykin, A. N. Kulak, F. C. Walsh, *Cryst. Growth Des.* 2010, **10**, 4421-4427.

[28] V. C. Stengl, S. Bakardjieva, *J. Phys. Chem. C* 2010, **114**, 19308-19317.

[29] J. E. Anthony, A. Facchetti, M. Heeney, S. R. Marder, X. Zhan, *Adv. Mater.* 2010, **22**, 3876-3892.